ACS APPLIED ELECTRONIC MATERIALS

pubs.acs.org/acsaelm Article

Understanding the Local Seebeck Coefficient of Carbon Nanotube Fibers Using the Photothermoelectric Effect

Shusen Liao, Yingru Song, Shengjie Yu, Lauren W. Taylor, Oliver S. Dewey, Matteo Pasquali, Junichiro Kono, Geoff Wehmeyer, and Douglas Natelson*

Cite This: https://doi.org/10.1021/acsaelm.4c01343 Read Online

ACCESS | Metrics & More | Article Recommendations | Supporting Information

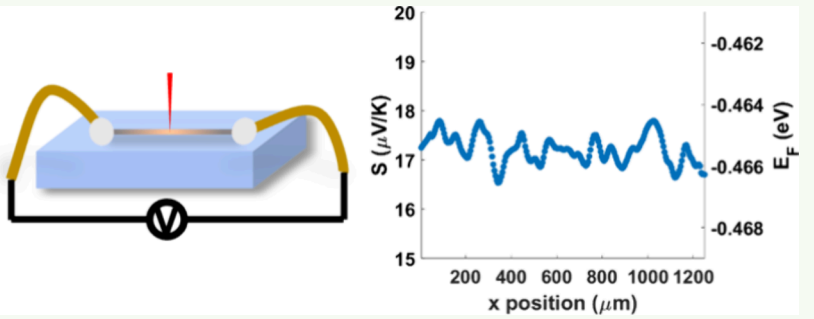

ABSTRACT: The applications of carbon nanotube fibers (CNTF) are broad because of their flexibility, high specific strength, and outstanding thermal and electrical properties. Although CNTFs have a hierarchical structure, their macroscopic properties, are usually discussed and investigated at the scale of the whole fiber, with a lack of understanding of the local properties, such as the Seebeck coefficient and the Fermi energy. Here, we study the variation of the Seebeck coefficient along the fibers by using the photothermoelectric (PTE) effect. The photovoltage is measured as a function of position, and the laser-induced temperature profile is obtained by a robust steady-state thermal model. The Seebeck coefficient as a function of position along the fiber can be obtained from the measured, spatially mapped photovoltage and temperature profile. We observe a correlation between the variation of the Seebeck coefficient and the shift of Raman modes, both related to the doping level and the Fermi energy. We find the Seebeck coefficient fluctuation in the pristine fiber is due to the nonuniformity of the doping level and the Fermi energy. With an established model to correlate the thermoelectric response and the Fermi energy, our PTE-based method can probe the Fermi energy fluctuation along the fiber with a resolution better than 1 meV, which is far beyond the capability of commercial Raman spectroscopy. This study shows a nondestructive method to quantify the uniformity of CNTF at the micrometer scale, key for fabricating more uniform and higher quality CNTF and generalizable to other conducting fiber systems.

KEYWORDS: *CNT fibers, Seebeck coefficient, photothermoelectric effect, Raman spectroscopy, doping level, Fermi level mapping*

INTRODUCTION

Carbon nanotube fibers (CNTF) are promising candidates for thermoelectric active cooling materials thanks to their unique combinations of electrical and thermal properties.[1,2] As the synthesis and fabrication of CNTF have improved, CNTF is reported to have a giant thermoelectric power factor as large as 14 ± 5 mW m^{-1} K^{-2} at room temperature,[3] which is the highest value for any carbon nanotube (CNT) system and approaches the highest values (about 30 mW m^{-1} K^{-2}) reported for 2D materials.[4,5] The outstanding electrical properties and thermoelectric response are typically discussed and investigated at the scale of the macroscopic fiber (~centimeter scale lengths or longer). However, due to the inherent microstructure, defects, and imperfections of the fibers introduced during fabrication, the local properties at different positions can deviate from the average values. At present, there is a relative lack of data on the variation of local properties along the fibers, though there have been some examinations of chemical heterogeneity[6] and mechanical properties[7] by nanoscale imaging.

Another method to reveal local variations within quasi-one-dimensional systems with large aspect ratios is the photothermoelectric (PTE) effect: a laser beam is focused on the sample at location x_0 to induce a temperature gradient $\nabla T(x, x_0)$ at all axial locations x, and an open-circuit voltage is established as a result of the Seebeck effect. The voltage can be written as

Received: July 30, 2024
Revised: October 9, 2024
Accepted: October 9, 2024

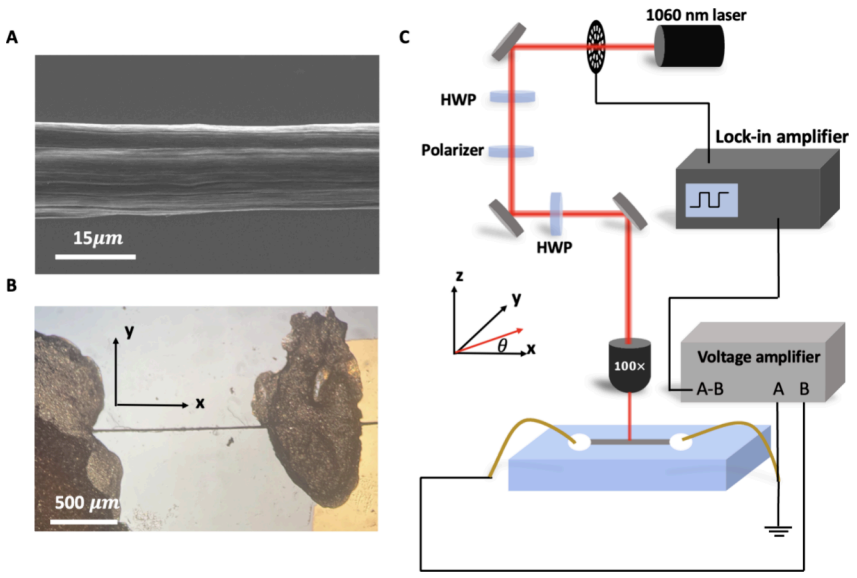

Figure 1. (A) Top-view SEM micrograph of the solution-spun CNTF. The CNTs in the fibers are densely packed and highly aligned. The average diameter of the fiber is 17.5 μm. The scale bar is 15 μm. (B) Optical micrograph of the device. The fiber is supported on a SiO_2/Si substrate. The fiber is connected to gold pads by silver paste for the electrical connection. The scale bar is 500 μm. (C) Schematic of the photovoltage measurement setup. The polarization angle of the incident 1060 nm light is θ relative to the x direction.

$$V(x_0) = -\int_0^L S(x)\nabla T(x, x_0)\mathrm{d}x \quad (1)$$

where $S(x)$ is the position-dependent Seebeck coefficient and L is the sample length. If the sample is perfectly uniform (i.e., $S(x) = S_{ave}$, a position-independent average), then the voltage V is zero if the temperature is identical at $x = 0$ and $x = L$. Therefore, any detected voltage signal indicates the nonuniformity of the system's Seebeck coefficient. By scanning the laser over the system, the photovoltage $V(x_0)$ as a function of laser position x_0 can be obtained. The temperature profile $T(x, x_0)$ induced by the laser and its gradient ∇T can be simulated or calculated by a model of thermal transport for the fiber and its surroundings, and the Seebeck coefficient $S(x)$ as a function of position can be found by numerical solution. The PTE effect has been used to show the nonuniformity of the Seebeck coefficient in metallic nanowires caused by grain boundaries[8] and impurities.[9] Several reports have established that the scanning PTE method can be used to probe the variation of the Seebeck coefficient of CNT films[10] and bundles.[11] These exciting prior studies showed that the technique can be used to map photovoltages at the ~100s of μV scale due to large Seebeck gradients (>5 μV/K over ~ mm length scales) arising due to position-dependent doping. From a technological perspective, device-level measurements have also shown that the PTE effect in CNT materials can be leveraged for efficient photodetectors,[12−17] motivating further investigation of PTE phenomena in CNT materials. This current work builds upon these prior studies by leveraging our recently developed lock-in-based scanning PTE technique to measure smaller order-of-magnitude photovoltages (single-digit μV) at higher spatial resolution (~5 μm) in high-performance CNT fibers, allowing quantification of Seebeck profiles with <1 μV/K sensitivity.

We use the PTE effect to map the Seebeck coefficient as a function of the axial position along CNTF at the micrometer scale. Compared with previous reports, we observe a correlation between the Seebeck coefficient and the shift of Raman modes along the fiber, both of which are related to the doping level. From the Seebeck coefficient, we use a previously developed band structure model to infer the variation of the doping level and to quantify the variation of the Fermi energy along as-spun and annealed fibers.[3] The inferred Fermi energy has a resolution higher than 1 meV, which is much better than the precision of prior optical methods. The Seebeck coefficient and the inferred Fermi energy provide detailed information about the fluctuation of the thermoelectric properties along the CNTF with high spatial resolution. This PTE effect-based method for probing variation of the Seebeck coefficient is nondestructive and will be helpful for fabricating more uniform and higher quality CNTF, as well as characterizing other quasi-1D systems.

RESULTS AND DISCUSSION

The CNTF in this study are very similar to the CNTF reported in ref 3, comprising double-wall CNTs, with average outer-wall and inner-wall diameters of 1.8 ± 0.2 and 0.9 ± 0.1 nm, respectively. The CNT length-to-diameter aspect ratio is 3600 ± 80, measured via extensional viscosity.[18] Continuous fibers are fabricated by a solution-spinning method.[19−21] A scanning electron microscopy (SEM) micrograph of the fiber is shown in Figure 1A. The CNTs within the fiber are densely packed and highly aligned, comparable to the CNTF in ref 20. The average diameter of the fiber is measured to be 17.5 μm from a cross-section view. The Raman spectra of the fiber are also measured (see Supporting Information, Section 1). The Raman G-to-D ratio is 50 at 532 nm laser excitation for the common G and D modes observed in CNTF,[3,19] implying a low defect density, and the low-frequency radial breathing mode (RBM) position is consistent with the CNT diameters.[22] As-made, these fibers are highly electrically conductive (~8 MS/m at room temperature) and are known to be strongly p-type doped by the remnant acid in the fiber.[3,20]

A 1−2 mm piece of the fabricated CNTF is cut to make a device. A photograph of a typical device is shown in Figure 1B. All of the devices are fabricated on Si wafers with a 2 μm thick SiO_2 layer. Gold contact pads with Ti adhesion layer are

https://doi.org/10.1021/acsaelm.4c01343
ACS Appl. Electron. Mater. XXXX, XXX, XXX−XXX

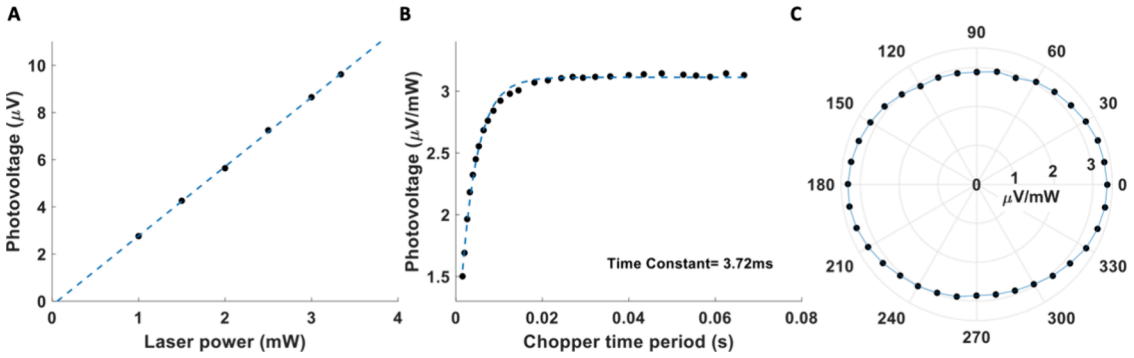

Figure 2. (A) PTE voltage (points) scales linearly with the laser power. The blue dashed line is the linear fit. (B) Normalized PTE voltage measured as a function of the chopper time period. The blue dashed curve is the exponential decay fit, which gives the time constant to be 3.7 ms. The millisecond time scale confirms that the voltage is from the PTE effect rather than a photovoltaic effect. (C) Laser polarization dependence of the PTE voltage. The voltage is the largest when the polarization is parallel to the axial direction (θ = 0°), and the voltage is the smallest when the polarization is perpendicular to the axial direction (θ = 90°). Line is interpolation.

evaporated, and the fiber is connected to the Au pads by silver paste. The device is wire-bonded at the Au pads for electrical measurements. The experimental setup for the PTE measurements is shown in Figure 1C. We use a 1060 nm laser as the excitation source. The laser is modulated by an optical chopper and focused at the fiber by a 100× objective with a 2.5 μm laser spot ($1/e^2$ radius). The intensity of the laser is controlled by a half-wave plate (HWP) and a polarizer. Another HWP controls the polarization angle, θ, the angle between laser polarization and the x direction. The photovoltage is first amplified by a voltage preamplifier and then measured by a lock-in amplifier synced to the chopper. The device can be moved in the x and y directions with two stepper motors, so the map of photovoltage can be obtained by scanning the excitation laser over the x−y plane with a user-defined pixel size. The spatial resolution of the measurement is limited by the laser spot size and the step size of the motors. All measurements are taken under ambient conditions at room temperature; our ability to perform the measurements in the air instead of in vacuum is advantageous for the application of the technique to broader materials sets that may display vacuum-sensitive desorption/dedeoping.

First, the laser spot position x_0 is fixed at the center of the fiber and the photovoltage is measured with different excitation laser power, as shown in Figure 2A. The photovoltage is linearly proportional to the input power, consistent with previous PTE investigations.[13,16] Therefore, the photovoltage is normalized by the laser power in the following discussion. To confirm the thermal origin of the photovoltage, we measure the photovoltage as a function of the chopper time period, as shown in Figure 2B. When the chopper period is short, the thermal quasi-steady state is not yet established, and the temperature rise does not reach its maximum value before the laser is blocked. As a result, the photovoltage is small. When the chopper period increases, the system has more time to respond, and the temperature rise is larger, so the photovoltage increases. At sufficiently long periods, the thermal steady-state is reached during the illumination and the temperature rise is maximized, leading to saturation of the photovoltage. The exponential fitting of the photovoltage as a function of the chopper period (dashed line in Figure 2B) gives a thermal time constant on the order of milliseconds, consistent with the previous PTE results.[11,13,16] This confirms that the photovoltage is due to the PTE effect rather than a photovoltaic effect, as such a purely electronic mechanism has time scales that are on the order of picoseconds.[23] The photovoltage also shows a slight laser polarization dependence, as shown in Figure 2C. The photovoltage is slightly smaller when the laser polarization is perpendicular to the fiber axial direction (θ = 90°) than when the laser polarization is parallel to the fiber (θ = 0°) with a ratio to be 0.85. This angle dependence is consistent with the high alignment of single CNTs along the fiber.[15,17,24]

Defining the x direction to be parallel to the fiber axis (Figure 1B,C), the photovoltage $V(x_0)$ can be written as eq 1, where x_0 is the laser position on the fiber. The Seebeck coefficient of the fiber $S(x)$ is a function of position along the fiber (but is taken to be temperature-independent considering the temperature rise is small in the PTE measurements), and the one-dimensional axial temperature gradient $\nabla T(x, x_0)$ is a function of both laser position and position along the fiber. In the map measurements, the fiber is discretized into different pixels with uniform spacing. Within each single pixel, the Seebeck coefficient is regarded to be constant. The photovoltage $V(x_j)$ when the laser is at pixel j on the fiber can be written as

$$V(x_j) = -\sum_{i=1}^{N} S_i \cdot \nabla T_i(x_j) \cdot \frac{L}{N} \tag{2}$$

where N is the total number of pixels, and S_i and $\nabla T_i(x_j)$ are the Seebeck coefficient and the temperature gradient at pixel i, respectively. The temperature profile and its gradient $\nabla T_i(x_j)$ are calculated by a thermal model (the Supporting Information, Section 2) that considers axial conduction, convection/radiation to the surroundings, and conduction into the supporting substrate. The thermal model imposes constant-temperature boundary conditions at x = 0 and x = L due to thermal anchoring by the silver paste. The fiber thermal conductivity k is assumed to be spatially uniform since the thermal conductivity is dominant by phonons at room temperature,[25] meaning that k is less sensitive to the doping level than S is (see also discussion below about measurement sensitivities). The laser whose spot size is smaller than the fiber diameter can induce a transverse (perpendicular to the fiber axis) temperature gradient, as the thermal conductivity is expected to be highly anisotropic.[26] Any transverse temperature gradient, however, has no coupling to the longitudinal photovoltage along the fiber, which only has contributions

https://doi.org/10.1021/acsaelm.4c01343
ACS Appl. Electron. Mater. XXXX, XXX, XXX−XXX

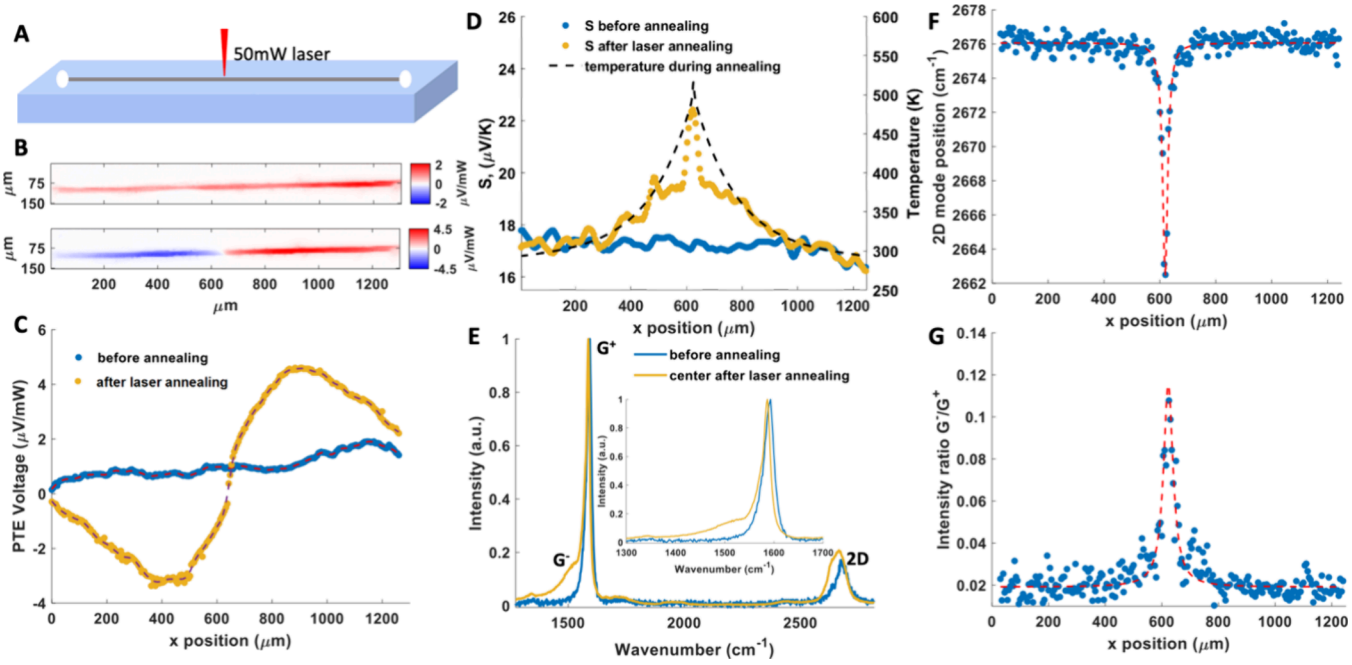

Figure 3. (A) Diagram of the laser annealing configuration. A 785 nm 50 mW laser irradiates the center of the fiber for 10 s to induce dedoping and modify $S(x)$. (B) PTE map measurements of the device before (top) and after (bottom) laser annealing. (C) PTE voltage as a function of x_0 position along the fiber before (blue) and after (yellow) the laser annealing. The PTE voltage is obtained from the map in (B). The dashed lines are the smooth curves fit to the PTE voltage and used to extract S. The magnitude of the PTE voltage is much larger after the local laser-induced annealing. (D) Left axis: calculated Seebeck coefficient as a function of x position before and after annealing. Right axis: simulated steady state temperature during the laser annealing. (E) Raman spectra of the fiber at $x \approx 620$ μm before and after the laser annealing show a red shift in the 2D band position and modified line shape of the G band. Inset: the spectra from 1300 to 1700 cm^{-1} including the G band. (F) Raman 2D band peak position as a function of the x position of the laser annealed fiber. The red shift can be clearly seen at $x \approx 620$ μm. (G) Raman intensity ratio between the G^- and G^+ bands as a function of x position of the laser annealed fiber. The broad G^- band appears at $x \approx 620$ μm. The red dashed curves in (F) and (G) are lines to guide the eyes. Comparing the Raman spectra and the Seebeck coefficient, we confirm that the increase in the Seebeck coefficient is caused by the shift of the doping level by the laser annealing.

from the cross-sectionally averaged longitudinal temperature gradient.

Based on the thermal model, the coefficient matrix ∇T of eq 2 has the rank of N-1, so the Seebeck coefficient S_i as a function of position is the summation of the relative Seebeck coefficient $S_{i,\mathrm{rel}}$ and the average Seebeck coefficient S_{ave}. We extract $S_{i,\mathrm{rel}}$ numerically from the measured photovoltage data using the methodology discussed in Supporting Information Section 3. We measure S_{ave} using a standard thermoelectric measurement (Supporting Information, Section 2), and we combine these parameters to find $S(x)$. The extracted Seebeck coefficient map is insensitive to perturbations in the spatially uniform k, or even to small position-dependent variations $k(x)$, as shown in Supporting Information Section 3. Fundamentally, our PTE experiments are much more sensitive to gradients in S than to gradients in k because the PTE signal vanishes if $S(x) = S_{\mathrm{ave}}$ for any ∇T (i.e., the PTE measurement is first-order sensitive to $\frac{dS}{dx}$ and second-order sensitive to thermal modeling terms like $\frac{dk}{dx}$ or the spatial gradients in the fiber cross-section dimensions). In Supporting Information Section 3, we also show the repeatability of the obtained Seebeck coefficient from different photovoltage measurements.

We demonstrate this methodology with different types of fiber samples. The PTE map measurements and Seebeck coefficient calculation are first performed on a fiber with a distinct feature in the Seebeck coefficient distribution deliberately introduced by localized laser annealing. It is known that thermal annealing of CNTF can dedope the material by evaporating the remnant acid and/or other adsorbed dopants such as water vapor and that this dedoping reduces their electrical conductivity and increases their average Seebeck response.[3,27] A high power (50 mW) 785 nm laser is focused at the center of the fiber for 10 s, as shown in Figure 3A. Induced by the laser, the temperature is increased to about 516 K (243 °C) at the center based on our thermal model (the Supporting Information, Section 4); this temperature rise is much larger than the temperature rises induced by the low-power (<3 mW) laser used in the PTE measurements. We expect the fiber to undergo modest dedoping by the brief exposure to elevated temperatures, resulting in an increase in the Seebeck coefficient near the center of the fiber within the heat-affected zone.

The PTE voltage maps of the device before and after laser annealing are measured, as shown in Figure 3B,C. Figure 3C shows the PTE voltage as a function of the x_0 position obtained by finding the maximum of the absolute value in each y-column in the PTE voltage maps in Figure 3B, C. Before annealing, the PTE voltage is small but nonzero, implying a nonuniform distribution of the Seebeck coefficient along the unannealed fiber. After laser annealing, we observe a large difference in the magnitude of the PTE voltage over the whole fiber. The Seebeck coefficient of the fiber both before and after annealing is calculated, as shown in Figure 3D. Before annealing, the Seebeck coefficient fluctuates around the 17.2 μV/K average value. After annealing, we observe an overall increase in the Seebeck coefficient from x = 350−850 μm. At

https://doi.org/10.1021/acsaelm.4c01343
ACS Appl. Electron. Mater. XXXX, XXX, XXX−XXX

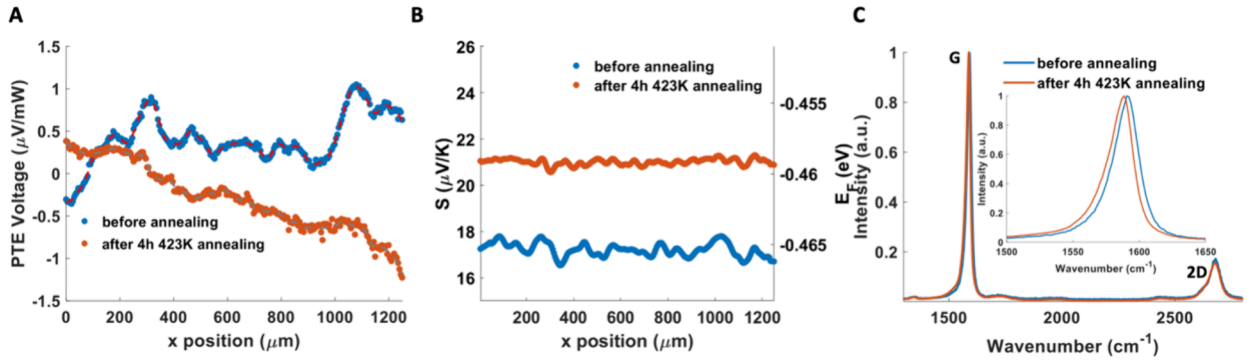

Figure 4. (A) PTE voltage as a function of x_0 position along the fiber before and after annealing at 423 K for 4 h in the furnace. The red and gray dashed lines are the smooth curves for the PTE voltage. (B) Calculated Seebeck coefficient and Fermi energy along the fiber before and after annealing. The Fermi energy is estimated based on the Seebeck coefficient via the model of ref 3. (C) Raman spectra of the fiber before and after annealing. Inset: the Raman spectra from 1500−1650 cm^{-1} including the G band. There is almost no shift in the 2D band, and the G band red shifts about 3 cm^{-1}.

the center location of $x \approx 620$ μm near the laser absorption location during annealing, the Seebeck coefficient increased by ~30%, to about 22.4 μV/K. The steady-state temperature profile during laser annealing is also simulated (the Supporting Information, Section 4) in Figure 3D to help explain the increase in the Seebeck coefficient: near the edge of the fiber ($x < 350$ and $x > 850$ μm), the temperature rise is low and it is insufficient to dedope the fiber or cause the increase in the Seebeck coefficient. In the range of $x = 350-850$ μm, the temperature rise is larger and leads to a measurable increase in the Seebeck coefficient. At the center, the temperature increases steeply to 516 K, which results in the increase of the Seebeck coefficient from about 19.5 to 22.4 μV/K in a short range of $x = 590-650$ μm.

We measure the Raman spectra of the fiber at $x \approx 620$ μm using 532 nm excitation before and after laser annealing, as shown in Figure 3E. The spectra show a large redshift (17 cm^{-1}) of the 2D band and a qualitative change in the line shape of the G band after annealing. A broad G^- band at about 1520 cm^{-1} appears after annealing, and there is a 3 cm^{-1} red shift in the G^+ band. The broad G^- band appears because the Fermi energy of the metallic CNTs shifts after annealing.[28−30] The red shift of Raman modes and the appearance of the G^- band further indicate the dedoping of the fiber after laser annealing.[27,30−32] More details about the analysis of the Raman spectrum are discussed in Supporting Information, Section 5.

The Raman spectra are also measured at each pixel along the fiber after laser annealing. The 2D band position and G^-/G^+ ratio as a function of x position are shown in Figure 3F,G. The red shift of the 2D band and the increase in the G^-/G^+ ratio can be seen at the center of the fiber. Comparing Figure 3D,F,G, we can see that the 2D band redshift and the increase of G^-/G^+ are more localized than the increase of the Seebeck coefficient. From $x = 350-590$ and $x = 650-850$ μm, the Raman spectra remain the same while the Seebeck coefficient increases. Combining the temperature profile during the laser annealing in Figure 3D, we can estimate the required temperature to see the Raman spectrum changes is about 460 K (287 °C).

We also measured the PTE map to investigate the Seebeck coefficient variation along a piece of the same fiber before and after global thermal annealing. Focusing first on the pristine fiber, the PTE voltage is shown in Figure 4A (blue curve), and the extracted Seebeck coefficient profile is shown in Figure 4B (blue curve). The Seebeck coefficient fluctuates around the 17.2 μV/K average value, and the standard deviation and range are 0.30 and 1.25 μV/K, respectively. To gain insight into the origins of the spatial variation, the whole fiber is annealed in a furnace with pressure below 100 mTorr for 4 h at 423 K (150 °C) (a thermal cycle determined not to harm the silver paste contacts). The PTE map measurement is performed again on the fiber, and then the Seebeck coefficient is calculated, as shown by the orange curves in Figure 4A,B respectively. After annealing, the average Seebeck coefficient is measured via global thermopower to be 21.0 μV/K. Our finding in Figure 4B shows that the spatial fluctuations are much smaller after annealing, with the standard deviation and range being 0.13 and 0.72 μV/K.

Raman measurements are consistent with these PTE observations, as well. The average Seebeck coefficient becomes larger after annealing because of the overall dedoping of the CNTF. The Raman spectra measured before and after annealing at 423 K for 4 h, as shown in Figure 4C, show that the G band red shifts about 3 cm^{-1}, consistent with dedoping of the fiber. However, unlike the laser annealing sample, the 423 K annealing sample shows no detectable shift in the 2D band. This finding is consistent with the result from Figure 3F and shows that an annealing temperature of 423 K is not large enough to result in a 2D band shift.

Given that the modest 423 K annealing temperature is unlikely to introduce changes in the structural arrangement or the strain of the fiber, the smaller fluctuation of the Seebeck coefficient after annealing suggests that the spatial variation in $S(x)$ likely originates from nonuniformities in the dopant concentration. We therefore attribute the lower spatial variation in $S(x)$ to a more uniform distribution of the doping level along the fiber for the remaining dopant in the fiber. Modeling the Seebeck coefficient fluctuation as caused by the nonuniform doping level, we can estimate the Fermi energy E_F as a function of position, as shown in Figure 4B right axis. This model uses the same correlation between the Seebeck coefficient and the Fermi energy described in a previous report[3] on these fibers. The Fermi energy of the fiber before and after annealing estimated from this model is −0.465 and −0.459 eV, and we can see fluctuations at the scale of 1 meV. Considering the 3 cm^{-1} shift in the G band of the Raman spectra (Figure 4C), we can estimate that at least a resolution of 3 cm^{-1}/0.006 (eV) = 0.5 cm^{-1} is needed for the Raman

https://doi.org/10.1021/acsaelm.4c01343
ACS Appl. Electron. Mater. XXXX, XXX, XXX−XXX

spectroscopy to probe the Fermi energy fluctuation in 1 meV. However, the 0.5 cm^{-1} spectral resolution is not available for most commercial Raman spectroscopy systems. Our PTE effect-based method can therefore detect finer variation of S and E_F along the fiber compared with Raman spectroscopy.

CONCLUSIONS

We use a lock-in-based PTE mapping approach to quantify the variation of the Seebeck coefficient along doped CNTF with high sensitivity (<1 μV/K). The inferred Seebeck coefficient as a function of position along the fiber is consistent with expectations for a deliberately modified doping level distribution for the laser annealing sample. We see a clear correlation between the Seebeck coefficient distribution and the Raman spectra as a function of position along the CNTF. This establishes that Seebeck's response is dominated by the local doping level. The data in this work shows that the lock-in-based PTE survey is more sensitive to small changes in the doping level and the Fermi energy than typical Raman spectroscopy. Comparing the PTE measurements and the Seebeck coefficient results before and after a mild isothermal annealing, we see an increase in the average Seebeck coefficient of the fiber due to the decrease in the doping level. The spatial variation of the Seebeck coefficient is smaller after annealing, likely because of the redistribution of dopants to a more uniform spatial distribution during the annealing process. From the Seebeck coefficient distribution, we can use a prior model connecting thermoelectric response and doping to calculate the Fermi energy along the fiber. This approach can be applied to other thermally one-dimensional systems given reliable thermal models for the temperature distribution $T(x, x_0)$. Such measurements provide information about the uniformity of the system's thermodynamic and electronic properties, which is helpful for synthesizing higher quality and more uniform materials.

METHODS

Derivation of PTE Temperature Profile. We consider one-dimensional (1D) steady-state heat conduction in the axial x direction of the CNTF due to point source heating from a laser beam. Because this heating period is substantially larger than the thermal time constant (Figure 2B), transient heat conduction effects are negligible, and the steady-state model is appropriate to describe the amplitude of the temperature rise. The 1D governing energy equation including radiation, convection, and thermal contact resistance that is used to find the steady-state temperature profile $T(x)$ is $\frac{d^2T}{dx^2} = m^2(T - T_0)$, where $m^2 \equiv \frac{1}{kA}\left(\pi Dh + \frac{1}{R_{contact}}\right)$ describes the effects of the losses to the surroundings, k is the fiber axial thermal conductivity, A is the fiber cross-sectional area, D is the fiber diameter, h is the heat transfer coefficient describing the combined effects of convection to the nearby air and radiation to the surroundings, $R_{contact}$ is the thermal contact resistance for a unit length between the CNTF and the silicon substrate (units of K. m/W), and T_0 is the ambient temperature. The analytical solving of the governing equation and more details of the derivation are discussed in Supporting Information Section 2.1.

Characterization of Fin Parameter mL in the PTE Experiment. The PTE measurements are performed in an open environment at room temperature. In this case, the convection, radiation, and heat conduction across the fiber−substrate interface are not negligible and require accurate characterization. We have utilized a steady-state Joule heating and resistance thermometry method to find the fin variable m. The CNTF samples are laid on the identical SiO_2/Si substrate as used in the PTE measurements to make sure the contact resistance is consistent, and measurements on multiple samples yield consistent values. With known A, L, k, and β of the CNTF sample, we can determine values of m. The detailed analytical derivation of the steady-state Joule heating method and the measured fin variable m values can be found in Supporting Information Section 2.2.

Thermal Conductivity Measurements. The thermal conductivity of the CNTF samples is the input parameter to the PTE measurements and characterization of the fin variable m. Prior to any measurement, we used Joule heating (steady state and three-omega) measurements to evaluate the thermal conductivity of the CNTF. In this experiment, the CNTF sample is suspended over the inner two silver paste electrodes and the measurements are performed in the vacuum chamber to prevent convection and conduction through the substrate. The detailed descriptions of the experimental setup and measured thermal conductivity can be found in the Supporting Information Section 2.3.

Average Seebeck Coefficient Measurements. To obtain the average Seebeck coefficient S_{ave}, we performed the standard steady-state measurements on both as-spun and annealed CNTFs. The CNTF samples are suspended over two heat-sunk Peltier modules which control the temperature difference between both ends of the CNTF. The details of the steady-state average Seebeck measurement and the data analysis are discussed in the Supporting Information, Section 2.5.

Raman Spectroscopy Measurements. The Raman spectroscopy is measured using a commercial Renishaw Raman system. A 532 nm laser with power smaller than 3 mW is focused on the fiber by a 50× , NA = 0.55 objective. The laser spot size ($1/e^2$ radius) is about 2.5 μm. The Raman map can be measured by moving the fiber with the sample holder in the sample plane. The pixel size can be customized, and for our map measurements, it is 5 μm. The PTE map is measured both before and after the Raman spectroscopy measurement to make sure that the fiber has no irreversible change during the Raman measurement. Laser annealing is also performed using the same Raman setup with a 50 mW 785 nm laser source.

Numerical Extraction of the Seebeck Coefficient. Eq 2 can be written in the matrix form as follows:

$$\begin{pmatrix} \nabla T_1(x_1) & \cdots & \nabla T_N(x_1) \\ \vdots & \ddots & \vdots \\ \nabla T_1(x_N) & \cdots & \nabla T_N(x_N) \end{pmatrix} \cdot \begin{pmatrix} S_1 \\ \vdots \\ S_N \end{pmatrix} = -\frac{N}{L} \cdot \begin{pmatrix} V(x_1) \\ \vdots \\ V(x_N) \end{pmatrix}$$

The ∇T matrix has a rank of N-1, so the general solution of the equations $S_i = S_{i,rel} + S_{ave}$. S_{ave} is the solution of the homogeneous linear equations $\nabla T \cdot S = 0$. S_{rel} is a particular solution of the above inhomogeneous linear equations. Consider the symmetric boundary condition of the temperature, for a perfectly uniform fiber ($S(x) = S_{ave}$), we have $V(x_0) = -\int_0^L S(x)\nabla T(x, x_0)dx = -S\int_0^L \nabla T(x, x_0)dx = S(T(x = 0) - T(x = L)) = 0$. As a result, $S_{ave} = C(1,1, ...,1)^T$, where C is a constant. S_{rel} can be numerically solved by $S_{rel} = -\frac{N}{L} \cdot \nabla T^{-1} V$, where ∇T^{-1} is the Moore-Penrose pseudoinverse of the matrix ∇T. The constant C can be obtained by setting the average of the Seebeck coefficient S_i to be the experimentally measured average Seebeck coefficient of the fiber. More details are described in Supporting Information Section 3.

ASSOCIATED CONTENT

Supporting Information

The Supporting Information is available free of charge at https://pubs.acs.org/doi/10.1021/acsaelm.4c01343.

Raman spectra of the fibers, thermal model of the fiber in PTE measurements, numerical extraction of the Seebeck coefficient and its robustness, simulated temperature profile during the laser annealing (PDF)

https://doi.org/10.1021/acsaelm.4c01343
ACS Appl. Electron. Mater. XXXX, XXX, XXX−XXX

AUTHOR INFORMATION

Corresponding Author

Douglas Natelson − *Carbon Hub, Applied Physics Graduate Program, Smalley-Curl Institute, Department of Physics and Astronomy, Department of Electrical and Computer Engineering, and Department of Materials Science and NanoEngineering, Rice University, Houston, Texas 77005, United States;* orcid.org/0000-0003-2370-9859; Email: natelson@rice.edu

Authors

Shusen Liao − *Carbon Hub, Applied Physics Graduate Program, Smalley-Curl Institute, and Department of Physics and Astronomy, Rice University, Houston, Texas 77005, United States;* orcid.org/0009-0009-6473-1199

Yingru Song − *Carbon Hub and Department of Mechanical Engineering, Rice University, Houston, Texas 77005, United States;* Present Address: Birck Nanotechnology Center and the School of Mechanical Engineering, Purdue University, West Lafayette, Indiana 47907, United States

Shengjie Yu − *Carbon Hub, Applied Physics Graduate Program, Smalley-Curl Institute, and Department of Electrical and Computer Engineering, Rice University, Houston, Texas 77005, United States*

Lauren W. Taylor − *Carbon Hub and Department of Chemical and Biomolecular Engineering, Rice University, Houston, Texas 77005, United States;* Present Address: Department of Chemical and Biomolecular Engineering, The Ohio State University, Columbus, Ohio 43210, United States.; orcid.org/0000-0002-6497-2795

Oliver S. Dewey − *Carbon Hub and Department of Chemical and Biomolecular Engineering, Rice University, Houston, Texas 77005, United States;* orcid.org/0000-0002-5779-6201

Matteo Pasquali − *Carbon Hub, Applied Physics Graduate Program, Smalley-Curl Institute, Department of Chemical and Biomolecular Engineering, Department of Chemistry, and Department of Materials Science and NanoEngineering, Rice University, Houston, Texas 77005, United States;* orcid.org/0000-0001-5951-395X

Junichiro Kono − *Carbon Hub, Applied Physics Graduate Program, Smalley-Curl Institute, Department of Physics and Astronomy, Department of Electrical and Computer Engineering, and Department of Materials Science and NanoEngineering, Rice University, Houston, Texas 77005, United States;* orcid.org/0000-0002-4195-0577

Geoff Wehmeyer − *Carbon Hub, Applied Physics Graduate Program, Smalley-Curl Institute, and Department of Mechanical Engineering, Rice University, Houston, Texas 77005, United States;* orcid.org/0000-0002-6764-7744

Complete contact information is available at: https://pubs.acs.org/10.1021/acsaelm.4c01343

Author Contributions

D.N., J.K., and G.W. conceived the study. O.S.D., L.W.T., and M.P. fabricated the CNT fibers. S.Y., S.L., J.K., and D.N. prepared the devices. S.L., Y.S., G.W., and D.N. performed experiments, analyzed the data, and built the thermal model. All authors contributed to the discussions of the results. S.L. wrote the manuscript with input from all authors.

Funding

This work is supported by the National Science Foundation (Grant # 2230727), the Robert A. Welch Foundation, C-1668 and C-1636, Department of Energy (DOE) Award DE-AR0001015 (Advanced Research Projects Agency—Energy), and by the Carbon Hub, a nonprofit institute which receives corporate funding from Shell, Mitsubishi Corporation (Americas), Prysmian, Saudi Aramco, Huntsman, ExxonMobil, Chevron, and SABIC.

Notes

The authors declare the following competing financial interest(s): M.P. and O.S.D. have a financial interest in DexMat, which commercializes solution-spun CNTF.

ACKNOWLEDGMENTS

We thank the staff and acknowledge the use of the facilities of the Shared Equipment Authority at Rice University. We thank Renjie Luo, Dr. Natsumi Komatsu, and Dr. Eldar Khabushev for the help in the experiments and discussion.

REFERENCES

(1) Zhang, Y.; Zhang, Q.; Chen, G. Carbon and Carbon Composites for Thermoelectric Applications. *Carbon Energy* **2020**, *2* (3), 408−436.

(2) Blackburn, J. L.; Ferguson, A. J.; Cho, C.; Grunlan, J. C. Carbon-Nanotube-Based Thermoelectric Materials and Devices. *Adv. Mater.* **2018**, *30* (11), No. 1704386.

(3) Komatsu, N.; Ichinose, Y.; Dewey, O. S.; Taylor, L. W.; Trafford, M. A.; Yomogida, Y.; Wehmeyer, G.; Pasquali, M.; Yanagi, K.; Kono, J. Macroscopic Weavable Fibers of Carbon Nanotubes with Giant Thermoelectric Power Factor. *Nat. Commun.* **2021**, *12* (1), 4931.

(4) Duan, J.; Wang, X.; Lai, X.; Li, G.; Watanabe, K.; Taniguchi, T.; Zebarjadi, M.; Andrei, E. Y. High Thermoelectricpower Factor in Graphene/HBN Devices. *Proc. Natl. Acad. Sci. U. S. A.* **2016**, *113* (50), 14272−14276.

(5) Shimizu, S.; Shiogai, J.; Takemori, N.; Sakai, S.; Ikeda, H.; Arita, R.; Nojima, T.; Tsukazaki, A.; Iwasa, Y. Giant Thermoelectric Power Factor in Ultrathin FeSe Superconductor. *Nat. Commun.* **2019**, *10* (1), 825.

(6) Mikhalchan, A.; Banas, A. M.; Banas, K.; Borkowska, A. M.; Nowakowski, M.; Breese, M. B. H.; Kwiatek, W. M.; Paluszkiewicz, C.; Tay, T. E. Revealing Chemical Heterogeneity of CNT Fiber Nanocomposites via Nanoscale Chemical Imaging. *Chem. Mater.* **2018**, *30* (6), 1856−1864.

(7) Wood, C. D.; Palmeri, M. J.; Putz, K. W.; Ho, G.; Barto, R.; Catherine Brinson, L. Nanoscale Structure and Local Mechanical Properties of Fiber-Reinforced Composites Containing MWCNT-Grafted Hybrid Glass Fibers. *Compos. Sci. Technol.* **2012**, *72* (14), 1705−1710.

(8) Evans, C. I.; Yang, R.; Gan, L. T.; Abbasi, M.; Wang, X.; Traylor, R.; Fan, J. A.; Natelson, D. Thermoelectric Response from Grain Boundaries and Lattice Distortions in Crystalline Gold Devices. *Proc. Natl. Acad. Sci. U. S. A.* **2020**, *117* (38), 23350−23355.

(9) Evans, C. I.; Gan, L. T.; Yang, R.; Abbasi, M.; Wang, X.; Traylor, R.; Fan, J. A.; Natelson, D. Detection of Trace Impurity Gradients in Noble Metals by the Photothermoelectric Effect. *J. Phys. Chem. C* **2021**, *125* (31), 17509−17517.

(10) St-Antoine, B. C.; Ménard, D.; Martel, R. Position Sensitive Photothermoelectric Effect in Suspended Single-Walled Carbon Nanotube Films. *Nano Lett.* **2009**, *9* (10), 3503−3508.

(11) Xu, S.; Zobeiri, H.; Hunter, N.; Zhang, H.; Eres, G.; Wang, X. Photocurrent in Carbon Nanotube Bundle: Graded Seebeck Coefficient Phenomenon. *Nano Energy* **2021**, *86*, No. 106054.

(12) Lu, X.; Sun, L.; Jiang, P.; Bao, X. Progress of Photodetectors Based on the Photothermoelectric Effect. *Adv. Mater.* **2019**, *31* (50), No. 1902044.

(13) Liu, Y.; Hu, Q.; Cao, Y.; Wang, P.; Wei, J.; Wu, W.; Wang, J.; Huang, F.; Sun, J.-L. High-Performance Ultrabroadband Photodetector Based on Photothermoelectric Effect. *ACS Appl. Mater. Interfaces* **2022**, *14* (25), 29077−29086.
(14) Wang, J.; Xie, Z.; Liu, J. A.; Yeow, J. T. W. Design of Room-Temperature Infrared Photothermoelectric Detectors Based on CNT/PEDOT:PSS Composites. *J. Mater. Chem. C Mater.* **2022**, *10* (40), 15105−15113.
(15) He, X.; Wang, X.; Nanot, S.; Cong, K.; Jiang, Q.; Kane, A. A.; Goldsmith, J. E. M.; Hauge, R. H.; Léonard, F.; Kono, J. Photothermoelectric p−n Junction Photodetector with Intrinsic Broadband Polarimetry Based on Macroscopic Carbon Nanotube Films. *ACS Nano* **2013**, *7* (8), 7271−7277.
(16) Erikson, K. J.; He, X.; Talin, A. A.; Mills, B.; Hauge, R. H.; Iguchi, T.; Fujimura, N.; Kawano, Y.; Kono, J.; Léonard, F. Figure of Merit for Carbon Nanotube Photothermoelectric Detectors. *ACS Nano* **2015**, *9* (12), 11618−11627.
(17) Zubair, A.; Wang, X.; Mirri, F.; Tsentalovich, D. E.; Fujimura, N.; Suzuki, D.; Soundarapandian, K. P.; Kawano, Y.; Pasquali, M.; Kono, J. Carbon Nanotube Woven Textile Photodetector. *Phys. Rev. Mater.* **2018**, *2* (1), No. 015201.
(18) Tsentalovich, D. E.; Ma, A. W. K.; Lee, J. A.; Behabtu, N.; Bengio, E. A.; Choi, A.; Hao, J.; Luo, Y.; Headrick, R. J.; Green, M. J.; Talmon, Y.; Pasquali, M. Relationship of Extensional Viscosity and Liquid Crystalline Transition to Length Distribution in Carbon Nanotube Solutions. *Macromolecules* **2016**, *49* (2), 681−689.
(19) Taylor, L. W.; Dewey, O. S.; Headrick, R. J.; Komatsu, N.; Peraca, N. M.; Wehmeyer, G.; Kono, J.; Pasquali, M. Improved Properties, Increased Production, and the Path to Broad Adoption of Carbon Nanotube Fibers. *Carbon N Y* **2021**, *171*, 689−694.
(20) Behabtu, N.; Young, C. C.; Tsentalovich, D. E.; Kleinerman, O.; Wang, X.; Ma, A. W. K.; Bengio, E. A.; ter Waarbeek, R. F.; de Jong, J. J.; Hoogerwerf, R. E.; Fairchild, S. B.; Ferguson, J. B.; Maruyama, B.; Kono, J.; Talmon, Y.; Cohen, Y.; Otto, M. J.; Pasquali, M. Strong, Light, Multifunctional Fibers of Carbon Nanotubes with Ultrahigh Conductivity. *Science (1979)* **2013**, *339* (6116), 182−186.
(21) Tsentalovich, D. E.; Headrick, R. J.; Mirri, F.; Hao, J.; Behabtu, N.; Young, C. C.; Pasquali, M. Influence of Carbon Nanotube Characteristics on Macroscopic Fiber Properties. *ACS Appl. Mater. Interfaces* **2017**, *9* (41), 36189−36198.
(22) Maultzsch, J.; Telg, H.; Reich, S.; Thomsen, C. Radial Breathing Mode of Single-Walled Carbon Nanotubes: Optical Transition Energies and Chiral-Index Assignment. *Phys. Rev. B* **2005**, *72* (20), No. 205438.
(23) Freitag, M.; Martin, Y.; Misewich, J. A.; Martel, R.; Avouris, Ph. Photoconductivity of Single Carbon Nanotubes. *Nano Lett.* **2003**, *3* (8), 1067−1071.
(24) Nanot, S.; Cummings, A. W.; Pint, C. L.; Ikeuchi, A.; Akiho, T.; Sueoka, K.; Hauge, R. H.; Léonard, F.; Kono, J. Broadband, Polarization-Sensitive Photodetector Based on Optically-Thick Films of Macroscopically Long, Dense and Aligned Carbon Nanotubes. *Sci. Rep.* **2013**, *3* (1), 1335.
(25) Hone, J.; Whitney, M.; Zettl, A. Thermal Conductivity of Single-Walled Carbon Nanotubes. *Synth. Met.* **1999**, *103* (1), 2498−2499.
(26) Yamaguchi, S.; Tsunekawa, I.; Komatsu, N.; Gao, W.; Shiga, T.; Kodama, T.; Kono, J.; Shiomi, J. One-Directional Thermal Transport in Densely Aligned Single-Wall Carbon Nanotube Films. *Appl. Phys. Lett.* **2019**, *115* (22), 223104.
(27) Tristant, D.; Zubair, A.; Puech, P.; Neumayer, F.; Moyano, S.; Headrick, R. J.; Tsentalovich, D. E.; Young, C. C.; Gerber, I. C.; Pasquali, M.; Kono, J.; Leotin, J. Enlightening the Ultrahigh Electrical Conductivities of Doped Double-Wall Carbon Nanotube Fibers by Raman Spectroscopy and First-Principles Calculations. *Nanoscale* **2016**, *8* (47), 19668−19676.
(28) Brown, S. D. M.; Jorio, A.; Corio, P.; Dresselhaus, M. S.; Dresselhaus, G.; Saito, R.; Kneipp, K. Origin of the Breit-Wigner-Fano Lineshape of the Tangential G-Band Feature of Metallic Carbon Nanotubes. *Phys. Rev. B* **2001**, *63* (15), No. 155414.
(29) Hároz, E. H.; Duque, J. G.; Rice, W. D.; Densmore, C. G.; Kono, J.; Doorn, S. K. Resonant Raman Spectroscopy of Armchair Carbon Nanotubes: Absence of Broad G^- Feature. *Phys. Rev. B* **2011**, *84* (12), No. 121403.
(30) Jorio, A.; Saito, R. Raman Spectroscopy for Carbon Nanotube Applications. *J. Appl. Phys.* **2021**, *129* (2), No. 021102.
(31) Das, A.; Sood, A. K.; Govindaraj, A.; Saitta, A. M.; Lazzeri, M.; Mauri, F.; Rao, C. N. R. Doping in Carbon Nanotubes Probed by Raman and Transport Measurements. *Phys. Rev. Lett.* **2007**, *99* (13), No. 136803.
(32) Das, A.; Pisana, S.; Chakraborty, B.; Piscanec, S.; Saha, S. K.; Waghmare, U. V.; Novoselov, K. S.; Krishnamurthy, H. R.; Geim, A. K.; Ferrari, A. C.; Sood, A. K. Monitoring Dopants by Raman Scattering in an Electrochemically Top-Gated Graphene Transistor. *Nat. Nanotechnol* **2008**, *3* (4), 210−215.

https://doi.org/10.1021/acsaelm.4c01343
ACS Appl. Electron. Mater. XXXX, XXX, XXX−XXX